






Strong coupling of Fabry-Pérot cavity mode, anapole, and exciton supported by an optical cavity with heterogeneous nano-optical metasurfaces

Junjie Li ^{1,*} Yang Cheng ^{1,*} Wei Liu ¹ Xiaoshan Liu,¹ Pingping Pan,¹ Jing Chen,² Zhengqi Liu ^{1,†} and Guiqiang Liu ^{1,‡}

¹College of Physics and Communication Electronics, Jiangxi Normal University, Nanchang 330022, Jiangxi, China

²College of Electronic and Optical Engineering, Nanjing University of Posts and Telecommunications, Nanjing 210023, China



(Received 23 January 2024; revised 28 April 2024; accepted 3 May 2024; published 20 May 2024)

Carefully designed metasurfaces can serve as effective platforms for strong coupling phenomena by the excitation of specific modes and the enhancement of light-matter interactions. However, strong coupling simultaneously involving Fabry-Pérot (FP) cavity modes, anapole states, and excitons has not been thoroughly explored. In this work, we numerically present the strong coupling of a FP cavity-anapole-exciton supported by a nano-optical metasurface of bulk WS₂-Si heterogeneous nanodisks inserted into a FP optical cavity. The excited multiorder FP cavity modes enable giant Rabi splittings with tunable population due to all generated odd-order FP cavity modes strongly coupling with the anapole state and exciton of bulk WS₂-Si heterogeneous nanodisks. Giant Rabi splittings of 643 and 335 meV are, respectively, achieved by the first-order FP and third-order FP cavity-anapole-exciton interactions. Our designed hybrid system provides a robust platform for exploring ultrahigh Rabi splittings and strong coupling of multiple optical responses in light-matter interactions.

DOI: [10.1103/PhysRevB.109.195425](https://doi.org/10.1103/PhysRevB.109.195425)

I. INTRODUCTION

Optical operations at nanoscale enable overcoming the limitations imposed by the diffraction limit in traditional optics [1–4]. By carefully designing metasurfaces, fascinating optical responses can be achieved owing to the significantly enhanced light-matter interactions [5–8], such as nonlinear optics [9,10], chiral optics [11,12], and strong coupling [13,14]. Strong coupling, a typical example of intense light-matter interactions, will happen between two or more excited modes in an optical system when the coherent energy exchange rate between light and matter exceeds the average dissipation rate of the modes [13–15]. Strong coupling allows the eventual formation of polaritons possessing both light and matter properties, manifested by an observable splitting in the spectrum [16]. So far, strong coupling phenomena have been extensively applied in ultrafast optical switches [17], Bose-Einstein condensations [18], low-threshold lasers [19], and so on. Various hybrid systems based on metal plasmonic metasurfaces have been established to generate strong coupling behaviors [20–24]. However, their practical applications might face certain limitations due to the large intrinsic ohmic losses, strong dispersion, and low-quality (Q) factors [25–27].

Dielectric metasurfaces, composed of high refractive index dielectric materials, exhibit low intrinsic losses [28,29]. Furthermore, their radiation losses can be further suppressed by the excitation of nonradiative states, such as anapole states [28–34] and bound states in the continuum (BICs) [35,36].

Anapoles originate from the destructive interference caused by uniform contributions of the out of phase electric dipole (ED) and toroidal dipole (TD) [32–34,37–40]. Anapoles are referred to as “states” and not as “modes” due to the fact that they are not the eigenmodes of scattering objects [30,32–34]. Anapole states can suppress far-field radiation and enhance near-field energy and have been extensively investigated in the strong coupling realm [41–44], e.g., anapole-plasmon-exciton coupling in the monolayer WSe₂-slotted Si nanodisk system [41], anapole-Fabry-Pérot (FP) cavity coupling in the FP cavity-Si nanocubes system [42], and anapole-exciton coupling in the molecular J -aggregate-Si nanodisk system [43]. However, fairly finite coupling strengths (<100 meV) [41] or Rabi splittings (≤ 192 meV) [41–43] restrict their further applications. To enhance the coupling strength, two effective approaches are developed: increasing the spatial overlap of electric fields or reducing the mode volume of resonators [44,45]. Recently, bulk WS₂ has attracted a lot of interest in both enhancing the spatial overlap of electric fields and reducing the mode volume due to its high real part of relative permittivity and superior exciton responses [45–47]. The use of bulk WS₂ enables the self-hybridization of the BIC exciton [45] and strong coupling of the anapole exciton [28]. The changeable oscillator strengths of WS₂ also contribute to realizing strong coupling and large Rabi splittings [48–50]. Thereby, bulk WS₂ provides an excellent platform for strong coupling involving excitons and large Rabi splittings.

Recently, FP cavities have also attracted a lot of attention in the strong coupling field due to the excited FP cavity modes and the highly confined electric field energy within the cavities [50–56]. Importantly, order-tunable FP cavity modes contribute to realizing multiple Rabi splittings. FP cavity based strong coupling, especially ternary strong coupling, has

*These authors contributed equally to this work.

[†]zliu@jxnu.edu.cn

[‡]liugq@jxnu.edu.cn

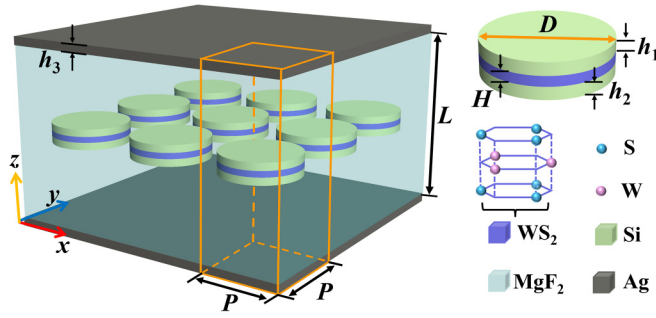


FIG. 1. Schematic diagram of the hybrid system with a nano-optical metasurface of WS₂-Si heterogeneous nanodisks embedded in the FP cavity and the molecular structure of bulk WS₂.

now drawn increasing attention [49,55,57]. For instance, Xie *et al.* studied cavity-assisted quasi-BIC-exciton strong coupling and achieved triple mixed states by embedding WS₂ elliptical cylinders in a FP cavity [49]. Zheng *et al.* illustrated ternary strong coupling of FP cavity-exciton-guided mode resonance (GMR) by inserting the FP cavity with a WS₂ photonic crystal [57]. However, strong coupling simultaneously involving FP cavity modes, anapole states, and excitons has not been thoroughly explored. Moreover, previous studies were mostly focused on the first-order FP (FP¹) [49,54,55] or third-order FP (FP³) [57] cavity mode in strong coupling systems, rarely involving different-order FP cavity modes simultaneously. Furthermore, giant Rabi splittings are also necessary for further applications of strong coupling.

In this work, we theoretically propose a hybrid system consisting of a nano-optical metasurface of bulk WS₂-Si heterogeneous nanodisks embedded in a FP optical cavity to realize FP cavity-anapole-exciton strong coupling with multiple Rabi splittings. Multiorder FP cavity modes are excited by adjusting the length of the FP cavity. The excited multiorder FP cavity modes are conducive to the realization of hybrid states, enabling the giant Rabi splittings with tunable quantity due to all generated odd-order FP cavity modes strongly coupling with the anapole state and exciton of heterogeneous nanodisks. The coherent effects involving FP¹ and FP³ cavity modes both exhibit large and tunable Rabi splittings due to their small mode volumes. Furthermore, the Rabi splittings can be modulated by the oscillator strength f_0 and giant Rabi splittings induced by strong coupling involving FP¹ (FP³) cavity modes reach 643 meV (335 meV). Our study provides a unique idea for constructing multi-optical-response based strong coupling systems and paves the way for enhancing light-matter interactions.

II. GEOMETRIC STRUCTURE AND NUMERICAL MODEL

We theoretically propose a nano-optical metasurface of heterogeneous nanodisks embedded in the center of a FP cavity. The schematic diagram is illustrated in Fig. 1. The FP optical cavity is composed of two Ag mirrors filled with MgF₂. The heterogeneous nanodisk consists of a bulk WS₂ nanodisk sandwiched between two Si nanodisks. The thicknesses for the three-layer nanodisks from top to bottom are $h_1 = 12$ nm, $H = 10$ nm, and $h_2 = 12$ nm. The diameter of the

nanodisks is $D = 160$ nm. The lattice constant is $P = 360$ nm and the thicknesses of the Ag mirrors are both $h_3 = 20$ nm. These parameters remain unchanged unless otherwise stated. The FP cavity length is denoted as L . To mitigate the increase in effective refractive index caused by the increased L , the background refractive index is set to 1.38. Si and WS₂ are used to support the excitation of the anapole state and exciton, the FP cavity is adopted to enable multiorder FP cavity modes by adjusting its length, and MgF₂ material is employed to support the heterogeneous nanodisks in the FP cavity.

Numerical calculations and electromagnetic field analyses are performed by the wave optics module in COMSOL MULTIPHYSICS software based on the finite element method (FEM) [58]. Theoretical analyses are carried out through the coupled mode theory (CMT) represented by the Hamiltonian matrix. The perfect matched layers are applied in the z direction and the Floquet periodic boundary conditions are applied in the x and y directions. An x -polarized plane wave source, located above the hybrid system, propagates along the negative direction of the z axis (i.e., perpendicular to the metasurface of the hybrid system). Two detectors are placed above and below the hybrid system to detect the transmission (T) and scattering (R), respectively. The total absorption (A) structure is obtained from $A = 1 - T - R$. The maximum mesh size is 42.7 nm.

The refractive indices are taken from the Palik database [59] for Si and Ag and from Ref. [60] for MgF₂. The artificial permittivity of bulk WS₂ is described by the Lorentz model [45,48,50,58],

$$\varepsilon = \varepsilon_0 + \frac{f_0 \omega_E^2}{\omega_E^2 - \omega^2 - i\Gamma_E \omega}, \quad (1)$$

where $\varepsilon_0 = 20$ is the background permittivity arising from high-energy transitions. $\hbar\omega_E = 2$ eV and $\hbar\Gamma_E = 50$ meV, respectively, represent the exciton transition energy and full linewidth. f_0 is the oscillator strength and its value can be varied [28,48–50]. Theoretically, $f_0 = 0$ corresponds to the pure background materials and $\varepsilon_0 = 1$ is associated with the pure excitonic materials. Here, for the bulk WS₂ with exciton contributions, the oscillator strength f_0 is set to 0.2 (a realistic value experimentally verified by Munkhbat *et al.* [50]) unless otherwise stated.

III. RESULTS AND DISCUSSION

A. Anapole state excitation in heterogeneous nanodisks

Initially, we consider the electromagnetic responses of heterogeneous nanodisks when the middle WS₂ nanodisks solely serve as the pure background materials without exciton contributions (i.e., $\varepsilon_0 = 20$ and $f_0 = 0$). A near-zero transmission dip with an evident redshift is clearly observed in Fig. 2(a) with the thickness increment of bulk WS₂ nanodisks. For the transmission dip (T_1) at $H = 10$ nm, two oppositely oriented circular currents form in the electric field distribution in the $x - y$ plane and a counterclockwise magnetic field occurs in the magnetic field distribution in the $y - z$ plane as shown in Fig. 2(b), verifying the excited anapole state of heterogeneous nanodisks.

To provide further insights into the physical mechanism of the anapole state, we calculated the scattering power of ED

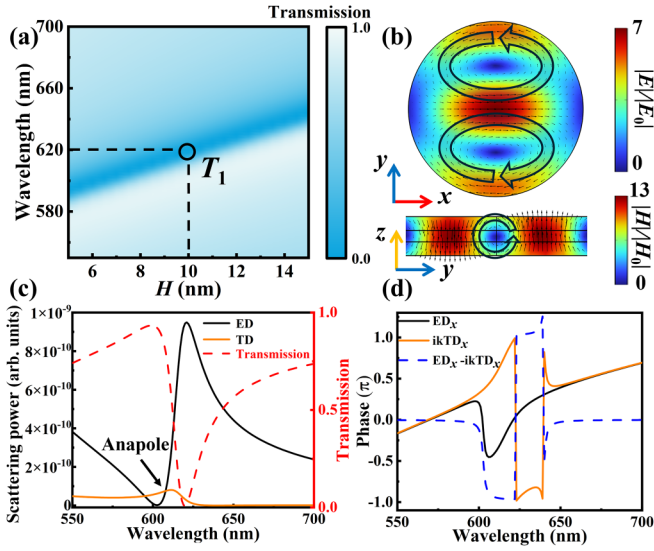


FIG. 2. (a) Transmission contour map of heterogeneous nanodisks with H . (b) Electromagnetic field distributions for the transmission dip at T_1 . (c) Scattering power of ED and TD moments and transmission spectrum of metasurface with $H = 10$ nm. (d) Normalized phases of ED and TD moments and their phase difference versus wavelength.

and TD moments via multipole decomposition in Cartesian coordinates. ED (\mathbf{P}) and TD (\mathbf{T}) moments as well as their corresponding scattering power (I_P) and (I_T) are defined as follows [61,62]:

$$\mathbf{P} = \frac{1}{i\omega} \int \mathbf{j} d^3r, \quad (2)$$

$$\mathbf{T} = \frac{1}{10c} \int [(\mathbf{r} \cdot \mathbf{j})\mathbf{r} - 2r^2\mathbf{j}] d^3r, \quad (3)$$

$$I_P = \frac{2\omega^4}{3c^3} |\mathbf{P}|^2, \quad (4)$$

$$I_T = \frac{2\omega^6}{3c^5} |\mathbf{T}|^2, \quad (5)$$

where ω is the angular frequency, \mathbf{r} is the position vector, \mathbf{j} is the current density vector, and c is the speed of light. Figure 2(c) plots the far-field scattering power of ED and TD moments as well as the transmission spectrum for the heterogeneous nanodisks with $H = 10$ nm. Evidently, the contributions of ED and TD moments are consistent at the intersection points of 595 and 608 nm. Normalized phases of the x component of these two moments (main contribution sources [63,64]) and their difference as a function of wavelength are plotted in Fig. 2(d). It is noteworthy that the normalized phase difference between ED_x and ikTD_x is close to -1 at 608 nm. Combined with the characteristics of far-field scattering power, it can conclude that the excitation condition depicted in Eq. (6) of the anapole state is satisfied [37,65]:

$$\mathbf{P} = ik\mathbf{T}. \quad (6)$$

In other words, the Cartesian ED and TD moments are out of phase and exhibit consistent scattering contributions. The working wavelength of the anapole state does not align with

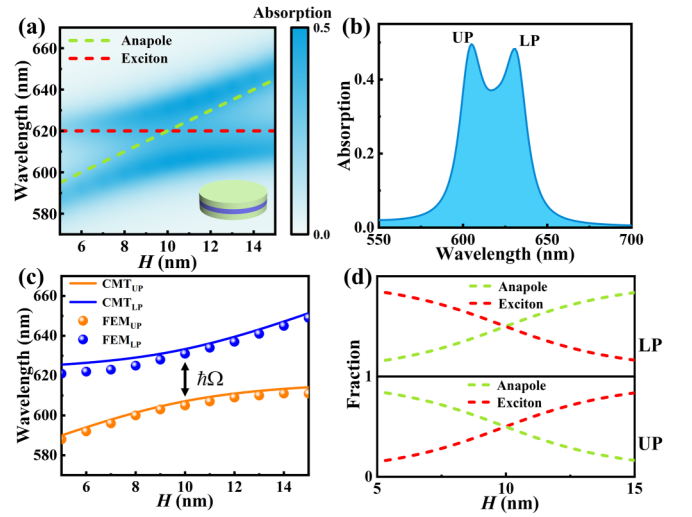


FIG. 3. (a) Absorption contour map of anapole-exciton hybrid states as a function of H . Inset: heterogeneous nanodisk. (b) Absorption spectrum of heterogeneous nanodisks with $H = 10$ nm. (c) Hybrid polariton branches calculated using FEM and CMT. (d) Hopfield coefficients for UP and LP polariton states contributed by anapole and exciton as a function of H .

the transmission dip wavelength due to the combined action of the anapole state and the metasurface array [28].

B. Strong coupling of anapole and exciton

Strong coupling between an anapole and an exciton is then considered by increasing f_0 to 0.2. In this work, only the A exciton at 620 nm of bulk WS₂ is considered. The B exciton at 496 nm is ignored due to the deviation from the resonant coupling region and the weak response induced by the thickness [49,57,60]. The absorption contour map of heterogeneous nanodisks with H is shown in Fig. 3(a). The uncoupled anapole resonance dip (green dashed line) and exciton response peak (red dashed line) are also shown here. Obviously, two hybrid energy states with a typical anticrossing behavior are discernible, indicating the appearance of strong coupling between anapole and exciton. Figure 3(b) describes the absorption spectrum of heterogeneous nanodisks with $H = 10$ nm. Two prominent absorption peaks, i.e., the upper polariton (UP) and lower polariton (LP) branches, are obtained via the interaction between the anapole state of heterogeneous nanodisks and the exciton of bulk WS₂. These hybrid states can be described by the coupled-mode resonator model expressed in a non-Hermitian Hamiltonian matrix with the intrinsic energy equation given by [66,67]

$$\hbar \begin{pmatrix} \omega_A - i\gamma_A & g_{A-E} \\ g_{A-E} & \omega_E - i\gamma_E \end{pmatrix} \begin{pmatrix} \alpha \\ \beta \end{pmatrix} = \hbar\omega_{\pm} \begin{pmatrix} \alpha \\ \beta \end{pmatrix}, \quad (7)$$

where $\hbar\omega_A$ and $\hbar\gamma_A$ are the resonance energy and half linewidth of the uncoupled anapole state, respectively. $\hbar\omega_E$ and $\hbar\gamma_E$ are the transition energy and half linewidth of the uncoupled exciton; g_{A-E} denotes the coupling strength of the anapole and exciton; α and β are the eigenvectors corresponding to the diagonalized Hamiltonian matrix, satisfying $|\alpha|^2 + |\beta|^2 = 1$. $\hbar\omega_+$ and $\hbar\omega_-$ are the two eigenvalues of

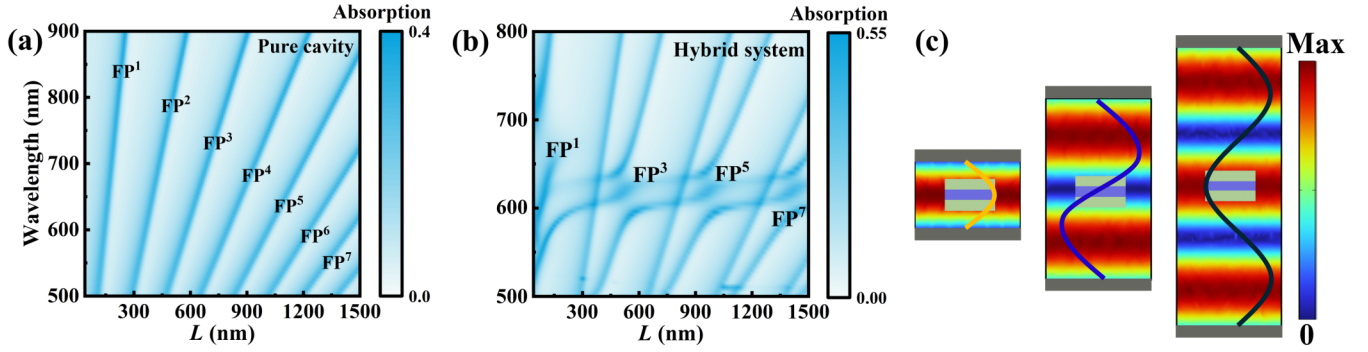


FIG. 4. (a) Absorption spectrum of pure FP cavity versus L . (b) Absorption spectrum of hybrid system versus L . (c) Electric field distribution of FP¹, FP², and FP³ cavity modes excited at different cavity lengths.

the diagonalized Hamiltonian matrix, corresponding to the energies of the UP and LP branches, and can be calculated by [63]

$$\begin{aligned} \hbar\omega_{\pm} = E_{\pm} = & \frac{\hbar}{2} \left\{ \omega_A + \omega_E - i\hbar\gamma_A - i\hbar\gamma_E \right. \\ & \left. \pm \sqrt{4g_{A-E}^2 + [\omega_A - \omega_E - (i\hbar\gamma_A - i\hbar\gamma_E)]^2} \right\}. \end{aligned} \quad (8)$$

When the resonance energy of the anapole equals the transition energy of the exciton, i.e., the detuning $(\hbar\omega_A - \hbar\omega_E)$ is zero, Eq. (8) satisfies $\text{Real}(\hbar\omega_A - \hbar\omega_E)_{\min}$, indicating the Rabi splitting [68]:

$$\hbar\Omega = \sqrt{4g_{A-E}^2 - (\hbar\gamma_A - \hbar\gamma_E)^2}. \quad (9)$$

Figure 3(c) presents the results of the coherent interaction between anapole and exciton calculated using FEM and CMT. It is easily obtained that the Rabi splitting is 84.4 meV. The coupling strength $g_{A-E} = 43.20$ meV is achieved via substituting $\hbar\Omega = 84.4$ meV, $\hbar\gamma_A = 43.45$ meV, and $\hbar\gamma_E = 25$ meV into Eq. (9). Moreover, the strong coupling conditions described in Eq. (10) are also satisfied, not only ensuring the coherent energy exchange rate exceeding the average dissipation rate but also guaranteeing the clear spectral splitting phenomena [68–70].

$$\begin{aligned} g_{A-E} &> \frac{1}{2}|\hbar\gamma_A - \hbar\gamma_E|, \\ \hbar\Omega &> \frac{1}{2}(\hbar\gamma_A + \hbar\gamma_E) \quad \text{or} \quad g_{A-E} > \frac{1}{4}\sqrt{(\hbar\gamma_A)^2 + (\hbar\gamma_E)^2}. \end{aligned} \quad (10)$$

Figure 3(d) is the fraction of the anapole state and the exciton in the LP and UP branches calculated by Eq. (7), which shows the process of coherent interaction between the anapole state and the exciton.

C. Strong coupling of FP cavity, anapole, and exciton

Figure 4(a) shows the absorption spectrum of the pure FP cavity with L increasing from 40 to 1500 nm. Multiple FP cavity modes, from FP¹ to seventh-order FP (FP⁷) cavity modes, are generated, which provide excellent conditions for multiple strong coupling. The FP cavity is then integrated

with the nano-optical metasurface of bulk WS₂-Si heterogeneous nanodisks; the absorption contour map is displayed in Fig. 4(b). Firstly, four prominent anticrossing behaviors verify the appearance of multiple strong coupling behaviors with multiple large Rabi splittings. Secondly, the Rabi splitting decreases with the increase in order of FP cavity mode due to the fact that the smaller mode volume can lead to the larger coupling strength. Lastly, the strong coupling behaviors only occur between odd-order FP (FP¹, FP³, FP⁵, and FP⁷) cavity modes, anapole states, and excitons. Even-order FP cavity modes do not participate in coherent interactions owing to the fact that FP cavity modes are typical standing wave modes [57]. Simple schematic diagrams are shown in Fig. 4(c) to illustrate the mode excitation principles of FP¹, FP², and FP³ cavity modes for the hybrid system with various cavity lengths. For the odd-order FP cavity modes, the heterogeneous nanodisks are precisely positioned at the wave crests with strong electric field energy. Strong electric field energy of odd-order FP cavity modes overlaps with those of the anapole state of heterogeneous nanodisks and the exciton of bulk WS₂ nanodisks and thus brings about FP cavity-anapole-exciton strong coupling and large Rabi splittings. For the even-order FP cavity modes, the heterogeneous nanodisks are located at the wave nodes where the electric field energy is zero, enabling the nonparticipation of even-order FP cavity modes in light-matter interactions.

To conveniently study the coupling effect between FP cavity modes, the anapole state, and the exciton, the lower odd-order FP (e.g., FP³ and FP¹) cavity modes are chosen to act as the preferred research objects. Figure 5(a) displays the spectral response of the hybrid system without excitonic contributions. It can be identified that the interaction between the FP³ cavity mode and the anapole state results in two hybridized energy branches, causing a large Rabi splitting of 196.5 meV. Noting that, the substantial increase in the effective refractive index of the hybrid system, induced by incorporating the heterogeneous nanodisks into the FP cavity, causes the redshift of the FP³ cavity mode (purple dashed line) [71]. Thereby, the zero-detuning point between the FP³ cavity mode and the anapole state occurs at $L = 520$ nm, not at the cavity length of $L = 601$ nm where the peak wavelength of the pure FP³ cavity mode is 620 nm (black dashed line).

Figure 5(b) shows the absorption spectrum of the hybrid energy states of a heterogeneous nanodisk-inserted FP cavity with excitonic contributions as a function of L . The red, green,

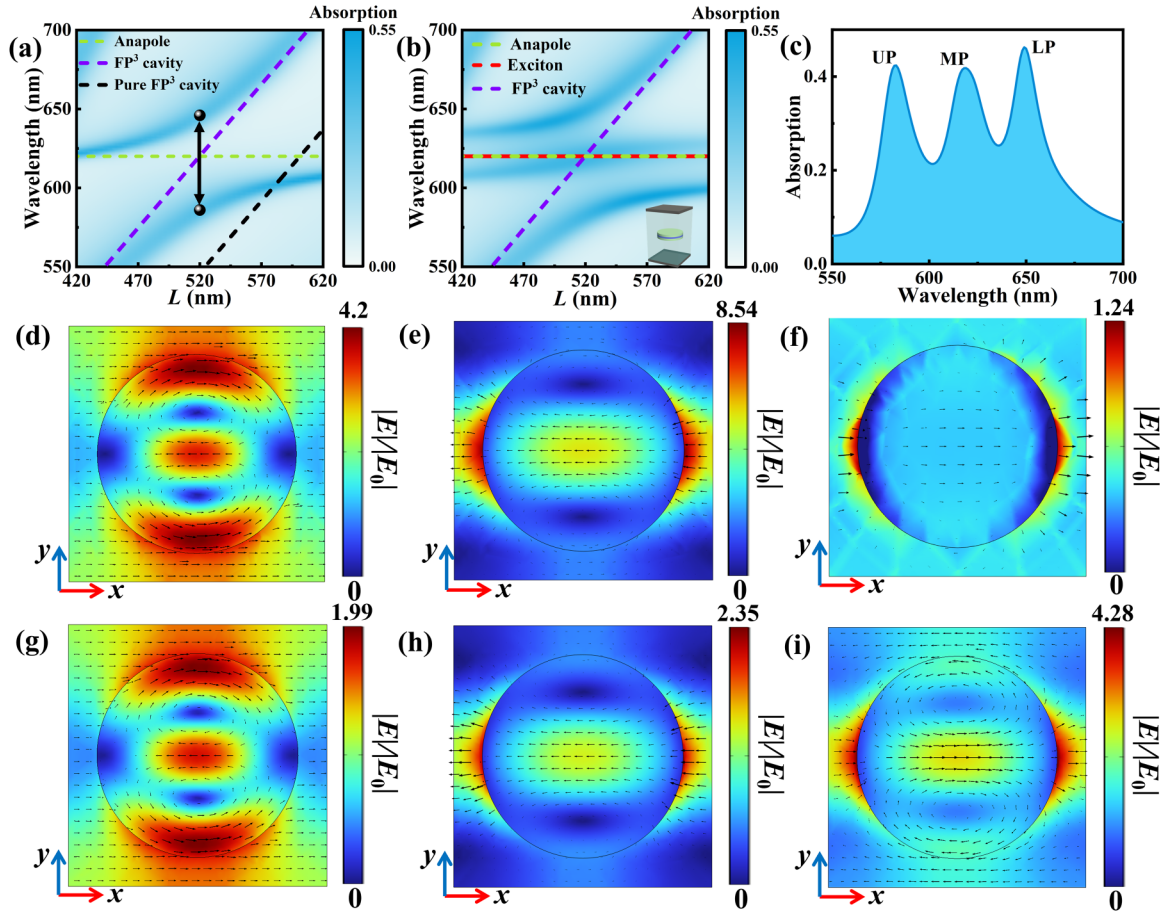


FIG. 5. (a) Absorption spectrum of the hybrid system with $f_0 = 0$. The black dashed line is the absorption peak wavelength of pure FP^3 cavity mode as L changes. (b) Absorption spectrum of the FP^3 cavity mode-anapole-exciton hybrid states as a function of L . Inset: unit cell. (c) Absorption spectrum of the hybrid system with $L = 520$ nm. Normalized electric field distributions of (d), (e) upper and lower branches at zero-detuning point of FP^3 cavity-anapole strong coupling; (f) exciton response of pure bulk WS_2 ; and (g)–(i) UP, LP, and MP branches at zero-detuning point of FP^3 cavity-anapole-exciton strong coupling.

and purple dashed lines represent the linear energy functions versus L for the uncoupled exciton, anapole state, and simulated FP^3 cavity response, respectively. It is easily observed that three absorption bands are formed, accompanied by a typical anticrossing behavior of the outer two branches and a nonlinear wavelength shift of the middle branch, indicating the coherent coupling among the FP^3 cavity mode, anapole state, and exciton. The collective interaction between the FP^3 cavity mode, anapole state, and exciton leads to the formation of the UP, middle polariton (MP), and LP branches, as shown in the absorption spectrum of the hybrid system with $L = 520$ nm in Fig. 5(c).

Normalized electric fields are also calculated. Figures 5(d) and 5(e), respectively, correspond to the upper and lower branches of FP^3 cavity-anapole strong coupling at the zero-detuning point; Figure 5(f) presents the electric field distribution of the exciton response of pure bulk WS_2 ; and Figs. 5(g)–5(i) are, respectively, related to the UP, LP, and MP branches at the zero-detuning point of FP^3 cavity-anapole-exciton strong coupling. Obviously, the electric field distribution patterns and displacement currents (black arrows) at the zero-detuning point for the UP and LP branches in

Figs. 5(g) and 5(h) are exactly the same as those observed in Figs. 5(d) and 5(e) except for the decreased intensity. Furthermore, the intensity, field distribution pattern, and displacement current of the MP branch in Fig. 5(i) are noticeably different from those observed in Fig. 5(f). These demonstrate that the excited exciton of bulk WS_2 is also involved in strong coupling, which consequently leads to the appearance of the middle polaritonic state, rather than the geometric resonance [72].

To further investigate the strong coupling of the FP^3 cavity, anapole, and exciton, a coupled-mode resonator model represented by a 3×3 Hamiltonian matrix is employed to describe the three hybrid states generated after the coherent interaction. The eigenenergy is given by [49,73]

$$\begin{aligned}
 & \hbar \begin{pmatrix} \omega_{\text{FP}} - i\gamma_{\text{FP}} & g_{\text{FP-A}} & g_{\text{FP-E}} \\ g_{\text{FP-A}} & \omega_{\text{A}} - i\gamma_{\text{A}} & g_{\text{A-E}} \\ g_{\text{FP-E}} & g_{\text{A-E}} & \omega_{\text{E}} - i\gamma_{\text{E}} \end{pmatrix} \begin{pmatrix} V_1 \\ V_2 \\ V_3 \end{pmatrix} \\
 & = \hbar \omega' \begin{pmatrix} V_1 \\ V_2 \\ V_3 \end{pmatrix}, \quad (11)
 \end{aligned}$$

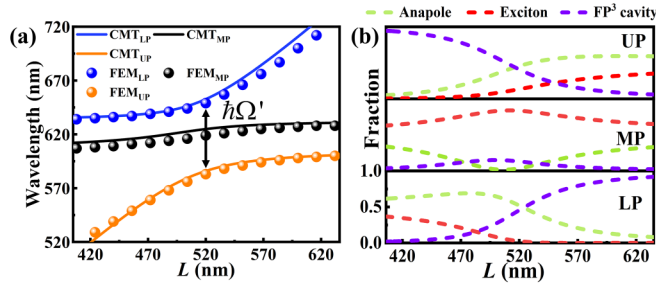


FIG. 6. (a) Hybrid polariton branches calculated using FEM and CMT. (b) Hopfield coefficients for UP, MP, and LP contributed by FP^3 cavity mode, anapole, and exciton as a function of L .

where $\hbar\omega_{FP}$ and $\hbar\gamma_{FP}$ are the resonance energy and half linewidth of the uncoupled FP^3 cavity mode, respectively. g_{A-E} , g_{FP-A} , and g_{FP-E} are the coupling strengths of the anapole-exciton, FP^3 cavity-anapole, and FP^3 cavity-exciton, respectively. V_1 , V_2 , and V_3 are eigenvectors corresponding to the third-order Hamiltonian matrix, satisfying $|V_1|^2 + |V_2|^2 + |V_3|^2 = 1$. The known values are brought into the resonator matrix model and the fitting results are shown in Fig. 6(a) (solid lines). The CMT fitting result of Rabi splitting is 216.38 meV, closely matching with the FEM calculated value of 216.3 meV (dots), again confirming the emergence of the middle polaritonic state rather than the geometric resonance [72]. Notably, the Rabi splitting induced by FP^3 cavity-anapole-exciton strong coupling is larger than those induced by anapole-exciton strong coupling in Fig. 3(c) and FP cavity-anapole strong coupling in Fig. 5(a), implying the excellent application prospects of strong coupling involving multiple optical responses.

To obtain better anticrossing behaviors, it is also necessary to satisfy the three-oscillator coupling criterion [60]:

$$\frac{\Omega'}{2} > W_{UP}\gamma_{UP} + W_{MP}\gamma_{MP} + W_{LP}\gamma_{LP}. \quad (12)$$

Here, W_{UP} , W_{MP} , and W_{LP} , respectively, represent the weights of three hybrid states (UP, MP, LP) resulting from the interaction of the FP^3 cavity, anapole, and exciton. γ_{UP} , γ_{MP} , and γ_{LP} correspond to the half linewidths of the three branches. The weights are defined as

$$\begin{aligned} W_{UP} &= \gamma_{UP}/(\gamma_{UP} + \gamma_{MP} + \gamma_{LP}), \\ W_{MP} &= \gamma_{MP}/(\gamma_{UP} + \gamma_{MP} + \gamma_{LP}), \\ W_{LP} &= \gamma_{LP}/(\gamma_{UP} + \gamma_{MP} + \gamma_{LP}). \end{aligned} \quad (13)$$

The eigenvectors are calculated from the Hamiltonian matrix and the Hopfield coefficients are determined as illustrated in Fig. 6(b). The mixed half linewidths are thus expressed as

$$\begin{aligned} \gamma_{UP} &= 40.91\%\gamma_{FP} + 45.64\%\gamma_A + 13.44\%\gamma_E, \\ \gamma_{MP} &= 13.05\%\gamma_{FP} + 3.49\%\gamma_A + 83.46\%\gamma_E, \\ \gamma_{LP} &= 45.42\%\gamma_{FP} + 52.09\%\gamma_A + 2.49\%\gamma_E. \end{aligned} \quad (14)$$

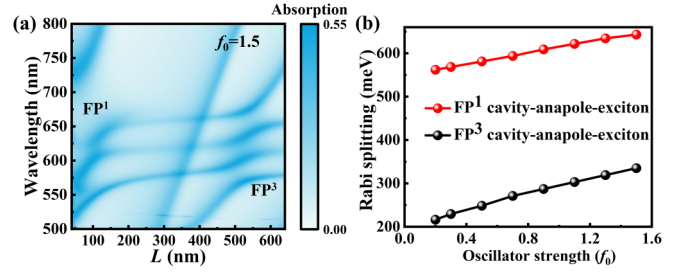


FIG. 7. (a) Absorption contour map of the hybrid system with $f_0 = 1.5$ ($40 \text{ nm} \leq L \leq 640 \text{ nm}$). (b) Variation trends of FP^1 and FP^3 cavity-anapole-exciton coupling induced Rabi splittings versus f_0 .

Then, substituting the results from Eq. (14) back into Eqs. (13) and (12), we find that the hybrid states satisfy the three-oscillator coupling criterion:

$$\frac{\Omega'}{2} > 37.21\%\gamma_{UP} + 23.40\%\gamma_{MP} + 39.39\%\gamma_{LP}. \quad (15)$$

Furthermore, the Rabi splittings induced by the FP^1 , FP^5 , and FP^7 cavity modes are also calculated in the cases of the zero-detuning cavity lengths based on the same calculation method as for the FP^3 cavity mode. The largest Rabi splitting is 562 meV for the FP^1 cavity mode in the case of a zero-detuning cavity length of $L = 86 \text{ nm}$, far larger than those achieved in other ternary coupling systems [41,49,55,57]. For the FP^5 and FP^7 cavity modes, corresponding Rabi splittings are 178.6 meV at $L = 978 \text{ nm}$ and 156.6 meV at $L = 1416 \text{ nm}$ [Fig. 4(b)]. The smallest Rabi splitting (156.6 meV) is still larger than that obtained in the FP cavity-exciton-GMR coupling system [57].

Figure 7(a) shows the absorption contour map of the hybrid states supported by the FP^1 and FP^3 cavity modes when $f_0 = 1.5$ ($40 \text{ nm} \leq L \leq 640 \text{ nm}$). Comparing with Fig. 4(b), the UP branches exhibit obvious blueshifts and the LP branches show prominent redshifts, resulting in larger Rabi splittings. In addition, the MP branches are split into two branches. It is because the increase in f_0 allows the enhanced excitonic response and residual excitons to emerge in the optical system [48,58]. These residual excitons reengage in coupling in the regions where the interactions between photons and excitons are not saturated, giving rise to the new middle polarization branches. Figure 7(b) presents the variation trends of Rabi splittings simultaneously involving the FP^1 and FP^3 cavity modes as a function of f_0 . Undoubtedly, the Rabi splittings both increase consistently as f_0 rises. As $f_0 = 1.5$, the FP^1 and FP^3 cavity-induced Rabi splittings are as high as 643 and 335 meV, respectively. Table I enumerates the strong coupling properties in different hybrid systems. It is evident that the Rabi splittings obtained here are far larger than those reported before [28,41,43,49,54,55,57,67,74,75], due to simultaneously involved exciton, anapole state, and FP cavity modes in strong coupling.

IV. CONCLUSIONS

In summary, we theoretically demonstrate a strong coupling system consisting of a nano-optical metasurface of bulk WS_2 -Si heterogeneous nanodisks inserted in a FP optical

TABLE I. Comparing hybrid structures, coupling modes/states, Rabi splittings, and f_0 in relevant works in the literature.

Hybrid structure	Coupling modes/states	Rabi splittings (meV)	f_0	Reference
Bulk WS ₂ -Si nanodisk	Anapole-exciton	151	0.4	[28]
Monolayer WSe ₂ -slotted Si nanodisk	Anapole-plasmon-exciton	159	No	[41]
Molecular <i>J</i> -aggregate ring-Si nanodisk	Anapole-exciton	161	No	[43]
Bulk WS ₂ embedded in FP cavity	FP ¹ cavity-quasi-BIC-exciton	464	1.5	[49]
Au nanowire embedded in FP cavity	FP ¹ cavity-magnetic plasmon	78	No	[54]
Monolayer WS ₂ -Au nanodisks in FP cavity	FP ¹ cavity-plasmon-exciton	535	No	[55]
Five-layer WS ₂ embedded in FP cavity	FP ³ cavity-exciton-GMR	120	No	[57]
Monolayer WS ₂ -SiN grating	Quasi-BIC-exciton	28.4	No	[67]
Organic molecules-Si nanoparticles	Mie surface lattice resonance exciton	~200	No	[74]
Molecular <i>J</i> -aggregate-Si nanodisks	Magnetic and electric Mie exciton	136/120	No	[75]
Bulk WS ₂ -Si nanodisks in FP cavity	FP ¹ /FP ³ cavity-anapole-exciton	643/335	1.5	This work

cavity. Multiorder FP cavity modes excited in this hybrid system are helpful to generate multimode hybrid states. Giant Rabi splittings with tunable quantity are achieved via strong coupling of odd-order FP cavity modes with the anapole and exciton. Strong coupling of the FP¹ (FP³) cavity, anapole, and exciton results in the giant Rabi splitting of 643 (335) meV. Our study provides a solid platform for achieving large Rabi splittings in strong coupling systems involving multiple optical responses.

ACKNOWLEDGMENTS

We acknowledge the financial support from the National Natural Science Foundation of China (NSFC) (Grants No. 62275112, No. 11804134, No. 51761015, and No. 11564017), the Natural Science Foundation of Jiangxi Province (Grants No. JXSQ2019201058 and No. 20232ACB201009), and the Graduate Student Innovation Foundation of Jiangxi Normal University (Grant No. YJS2023105).

- [1] J. Hu, S. Bandyopadhyay, Y.-H. Liu, and L.-Y. Shao, A review on metasurface: From principle to smart metadevices, *Front. Phys.* **8**, 586087 (2021).
- [2] C. Zhou, S. Li, Y. Wang, and M. Zhan, Multiple toroidal dipole Fano resonances of asymmetric dielectric nanohole arrays, *Phys. Rev. B* **100**, 195306 (2019).
- [3] F. Y. Han and P. K. Liu, Terahertz near-field metasurfaces: Amplitude-phase combined steering and electromagnetostatic dual-field superfocusing, *Adv. Opt. Mater.* **8**, 1901331 (2020).
- [4] L. Chen, Z. Shao, J. Liu, and D. Tang, Reflective quasi-continuous metasurface with continuous phase control for light focusing, *Materials* **14**, 2147 (2021).
- [5] S. Li, C. Zhou, T. Liu, and S. Xiao, Symmetry-protected bound states in the continuum supported by all-dielectric metasurfaces, *Phys. Rev. A* **100**, 063803 (2019).
- [6] K. Koshelev, S. Leshchov, M. Liu, A. Bogdanov, and Y. Kivshar, Asymmetric metasurfaces with high-resonances governed by bound states in the continuum, *Phys. Rev. Lett.* **121**, 193903 (2018).
- [7] Y. Zhang, D. Chen, W. Ma, S. You, J. Zhang, M. Fan, and C. Zhou, Active optical modulation of quasi-BICs in Si-VO₂ hybrid metasurfaces, *Opt. Lett.* **47**, 5517 (2022).
- [8] K. Bi, Q. Wang, J. Xu, L. Chen, C. Lan, and M. Lei, All-dielectric metamaterial fabrication techniques, *Adv. Opt. Mater.* **9**, 2001474 (2020).
- [9] K.-H. Kim and W.-S. Rim, Anapole resonances facilitated by high-index contrast between substrate and dielectric nanodisk enhance vacuum ultraviolet generation, *ACS Photon.* **5**, 4769 (2018).
- [10] S. Xiao, M. Qin, J. Duan, F. Wu, and T. Liu, Polarization-controlled dynamically switchable high-harmonic generation from all-dielectric metasurfaces governed by dual bound states in the continuum, *Phys. Rev. B* **105**, 195440 (2022).
- [11] M. V. Gorkunov, A. A. Antonov, and Y. S. Kivshar, Metasurfaces with maximum chirality empowered by bound states in the continuum, *Phys. Rev. Lett.* **125**, 093903 (2020).
- [12] H. Barkaoui, K. Du, Y. Chen, S. Xiao, and Q. Song, Merged bound states in the continuum for giant superchiral field and chiral mode splitting, *Phys. Rev. B* **107**, 045305 (2023).
- [13] Y. Niu, L. Gao, H. Xu, and H. Wei, Strong coupling of multiple plasmon modes and excitons with excitation light controlled active tuning, *Nanophotonics* **12**, 735 (2023).
- [14] P. Xie, D. Li, Y. Chen, P. Chang, H. Zhang, J. Yi, and W. Wang, Enhanced coherent interaction between monolayer WS₂ and film-coupled nanocube open cavity with suppressed incoherent damping pathway, *Phys. Rev. B* **102**, 115430 (2020).
- [15] M. Qin, S. Xiao, W. Liu, M. Ouyang, T. Yu, T. Wang, and Q. Liao, Strong coupling between excitons and magnetic dipole quasi-bound states in the continuum in WS₂-TiO₂ hybrid metasurfaces, *Opt. Express* **29**, 18026 (2021).
- [16] K. As'ham, I. Al-Ani, M. Alaloul, S. Abdo, A. Abdulghani, W. Lei, H. T. Hattori, L. Huang, and A. E. Miroshnichenko, Enhanced strong coupling in the hybrid dielectric-metallic nanoresonator and WS₂ monolayer, *Phys. Rev. Appl.* **19**, 054049 (2023).
- [17] W. Chen, K. M. Beck, R. Bückler, M. Gullans, M. D. Lukin, H. Tanji-Suzuki, and V. Vuletić, All-optical switch and transistor gated by one stored photon, *Science* **341**, 768 (2013).
- [18] J. D. Plumhof, T. Stöferle, L. Mai, U. Scherf, and R. F. Mahrt, Room-temperature Bose-Einstein condensation of cavity exciton-polaritons in a polymer, *Nat. Mater.* **13**, 247 (2014).

- [19] S. Wu, S. Buckley, J. R. Schaibley, L. Feng, J. Yan, D. G. Mandrus, F. Hatami, W. Yao, J. Vučković, A. Majumdar, and X. Xu, Monolayer semiconductor nanocavity lasers with ultralow thresholds, *Nature (London)* **520**, 69 (2015).
- [20] J. Sun, Y. Li, H. Hu, W. Chen, D. Zheng, S. Zhang, and H. Xu, Strong plasmon–exciton coupling in transition metal dichalcogenides and plasmonic nanostructures, *Nanoscale* **13**, 4408 (2021).
- [21] G. Zengin, M. Wersäll, S. Nilsson, T. J. Antosiewicz, M. Käll, and T. Shegai, Realizing strong light-matter interactions between single-nanoparticle plasmons and molecular excitons at ambient conditions, *Phys. Rev. Lett.* **114**, 157401 (2015).
- [22] J. Sun, H. Hu, D. Zheng, D. Zhang, Q. Deng, S. Zhang, and H. Xu, Light-emitting plexciton: Exploiting plasmon–exciton interaction in the intermediate coupling regime, *ACS Nano* **12**, 10393 (2018).
- [23] P. Jiang, G. Song, Y. Wang, C. Li, L. Wang, and L. Yu, Tunable strong exciton–plasmon–exciton coupling in WS_2 - J -aggregates–plasmonic nanocavity, *Opt. Express* **27**, 16613 (2019).
- [24] L. Yang, X. Xie, J. Yang, M. Xue, S. Wu, S. Xiao, F. Song, J. Dang, S. Sun, Z. Zuo, J. Chen, Y. Huang, X. Zhou, K. Jin, C. Wang, and X. Xu, Strong light–matter interactions between gap plasmons and two-dimensional excitons under ambient conditions in a deterministic way, *Nano Lett.* **22**, 2177 (2022).
- [25] L. Cong, M. Manjappa, N. Xu, I. Al-Naib, W. Zhang, and R. Singh, Fano resonances in terahertz metasurfaces: A figure of merit optimization, *Adv. Opt. Mater.* **3**, 1537 (2015).
- [26] D. Ö. Güney, T. Koschny, and C. M. Soukoulis, Reducing ohmic losses in metamaterials by geometric tailoring, *Phys. Rev. B* **80**, 125129 (2009).
- [27] J. Wang, J. Kühne, T. Karamanos, C. Rockstuhl, S. A. Maier, and A. Tittl, All-dielectric crescent metasurface sensor driven by bound states in the continuum, *Adv. Funct. Mater.* **31**, 2104652 (2021).
- [28] J. Wang, W. Yang, G. Sun, Y. He, P. Ren, and Z. Yang, Boosting anapole–exciton strong coupling in all-dielectric heterostructures, *Photon. Res.* **10**, 1744 (2022).
- [29] A. A. Basharin, V. Chuguevsky, N. Volsky, M. Kafesaki, and E. N. Economou, Extremely high Q -factor metamaterials due to anapole excitation, *Phys. Rev. B* **95**, 035104 (2017).
- [30] F. Monticone, D. Sounas, A. Krasnok, and A. Alu, Can a nonradiating mode be externally excited? Nonscattering states versus embedded eigenstates, *ACS Photon.* **6**, 3108 (2019).
- [31] B. Luk'yanchuk, R. Paniagua-Domínguez, A. I. Kuznetsov, A. E. Miroshnichenko, and Y. S. Kivshar, Hybrid anapole modes of high-index dielectric nanoparticles, *Phys. Rev. A* **95**, 063820 (2017).
- [32] E. Zanganeh, A. Evlyukhin, A. Miroshnichenko, M. Song, E. Nenasheva, and P. Kapitanova, Anapole meta-atoms: Nonradiating electric and magnetic sources, *Phys. Rev. Lett.* **127**, 096804 (2021).
- [33] A. A. Basharin, E. Zanganeh, A. K. Ospanova, P. Kapitanova, and A. B. Evlyukhin, Selective superinvisibility effect via compound anapole, *Phys. Rev. B* **107**, 155104 (2023).
- [34] K. Baryshnikova, D. Filonov, C. Simovski, A. Evlyukhin, A. Kadochkin, E. Nenasheva, P. Ginzburg, and A. S. Shalin, Giant magnetoelectric field separation via anapole-type states in high-index dielectric structures, *Phys. Rev. B* **98**, 165419 (2018).
- [35] J. Huang, B. Meng, L. Chen, X. Wang, X. Qu, M. Fan, and C. Zhou, Light trapping and manipulation of quasibound states in continuum $Ge_2Sb_2Se_4Te$ metasurfaces, *Phys. Rev. B* **106**, 045416 (2022).
- [36] S. I. Azzam and A. V. Kildishev, Photonic bound states in the continuum: From basics to applications, *Adv. Optical Mater.* **9**, 2001469 (2020).
- [37] A. E. Miroshnichenko, A. B. Evlyukhin, Y. F. Yu, R. M. Bakker, A. Chipouline, A. I. Kuznetsov, B. Luk'yanchuk, B. N. Chichkov, and Y. S. Kivshar, Nonradiating anapole modes in dielectric nanoparticles, *Nat. Commun.* **6**, 8069 (2015).
- [38] K. Koshelev, G. Favraud, A. Bogdanov, Y. Kivshar, and A. Fratallocchi, Nonradiating photonics with resonant dielectric nanostructures, *Nanophotonics* **8**, 725 (2019).
- [39] K. V. Baryshnikova, D. A. Smirnova, B. S. Luk'yanchuk, and Y. S. Kivshar, Optical anapoles: Concepts and applications, *Adv. Opt. Mater.* **7**, 1801350 (2019).
- [40] T. Yezekyan, V. A. Zenin, J. Beermann, and S. I. Bozhevolnyi, Anapole states in gap-surface plasmon resonators, *Nano Lett.* **22**, 6098 (2022).
- [41] K. As'ham, I. Al-Ani, L. Huang, A. E. Miroshnichenko, and H. T. Hattori, Boosting strong coupling in a hybrid WSe_2 monolayer–anapole–plasmon system, *ACS Photon.* **8**, 489 (2021).
- [42] W. Liu, Y. Tang, Z. Liu, J. Li, Y. Cheng, and G. Liu, Realizing anapole-FP cavity strong coupling in a silicon-based metasurface hybrid system, *IEEE Photon. J.* **15**, 6501005 (2023).
- [43] S.-D. Liu, J.-L. Fan, W.-J. Wang, J.-D. Chen, and Z.-H. Chen, Resonance coupling between molecular excitons and nonradiating anapole modes in silicon nanodisk- J -aggregate heterostructures, *ACS Photon.* **5**, 1628 (2018).
- [44] B. Gerislioglu and A. Ahmadivand, Theoretical study of photoluminescence spectroscopy of strong exciton-polariton coupling in dielectric nanodisks with anapole states, *Mater. Today Chem.* **16**, 100254 (2020).
- [45] T. Weber, L. Kühner, L. Sortino, A. Ben Mhenni, N. P. Wilson, J. Kühne, J. J. Finley, S. A. Maier, and A. Tittl, Intrinsic strong light-matter coupling with self-hybridized bound states in the continuum in van der Waals metasurfaces, *Nat. Mater.* **22**, 970 (2023).
- [46] R. Verre, D. G. Baranov, B. Munkhbat, J. Cuadra, M. Käll, and T. Shegai, Transition metal dichalcogenide nanodisks as high-index dielectric Mie nanoresonators, *Nat. Nanotechnol.* **14**, 679 (2019).
- [47] Y. Li, A. Chernikov, X. Zhang, A. Rigosi, H. M. Hill, A. M. van der Zande, D. A. Chenet, E.-M. Shih, J. Hone, and T. F. Heinz, Measurement of the optical dielectric function of monolayer transition-metal dichalcogenides: MoS_2 , $MoSe_2$, WS_2 , and WSe_2 , *Phys. Rev. B* **90**, 205422 (2014).
- [48] S. You, Y. Zhang, M. Fan, S. Luo, and C. Zhou, Strong light–matter interactions of exciton in bulk WS_2 and a toroidal dipole resonance, *Opt. Lett.* **48**, 1530 (2023).
- [49] P. Xie, Q. Ding, Z. Liang, S. Shen, L. Yue, H. Zhang, and W. Wang, Cavity-assisted boosting of self-hybridization between excitons and photonic bound states in the continuum in multilayers of transition metal dichalcogenides, *Phys. Rev. B* **107**, 075415 (2023).
- [50] B. Munkhbat, D. G. Baranov, M. Stührenberg, M. Wersäll, A. Bisht, and T. Shegai, Self-hybridized exciton-polaritons in

- multilayers of transition metal dichalcogenides for efficient light absorption, *ACS Photon.* **6**, 139 (2018).
- [51] P. Xie, Y. Deng, L. Zeng, Z. Liang, S. Shen, Q. Ding, H. Zhang, Z. Zhou, and W. Wang, Tunable interactions of quasibound states in the continuum with cavity mode in a metasurface-microcavity hybrid, *Phys. Rev. B* **106**, 165408 (2022).
- [52] D. G. Baranov, B. Munkhbat, E. Zhukova, A. Bisht, A. Canales, B. Rousseaux, G. Johansson, T. J. Antosiewicz, and T. Shegai, Ultrastrong coupling between nanoparticle plasmons and cavity photons at ambient conditions, *Nat. Commun.* **11**, 2715 (2020).
- [53] J. Yang, H. Zhang, T. Wang, I. De Leon, R. P. Zaccaria, H. Qian, H. Chen, and G. Wang, Strong coupling of tamm plasmons and Fabry-Perot modes in a one-dimensional photonic crystal heterostructure, *Phys. Rev. Appl.* **18**, 014056 (2022).
- [54] J. Chen, T. Zhang, C. Tang, P. Mao, Y. Liu, Y. Yu, and Z. Liu, Optical magnetic field enhancement via coupling magnetic plasmons to optical cavity modes, *IEEE Photon. Technol. Lett.* **28**, 1529 (2016).
- [55] A. Bisht, J. Cuadra, M. Wersäll, A. Canales, T. J. Antosiewicz, and T. Shegai, Collective strong light-matter coupling in hierarchical microcavity-plasmon-exciton systems, *Nano Lett.* **19**, 189 (2018).
- [56] Z. Sun and Y. Fang, Fabry-Pérot interference cavity length tuned by plasmonic nanoparticle metasurface for nanophotonic device design, *ACS Appl. Nano Mater.* **3**, 10732 (2020).
- [57] H. Zheng, Y. Bai, Q. Zhang, and S. Liu, Multi-mode strong coupling in Fabry-Pérot cavity-WS₂ photonic crystal hybrid structures, *Opt. Express* **31**, 24976 (2023).
- [58] M. Qin, J. Duan, S. Xiao, W. Liu, T. Yu, T. Wang, and Q. Liao, Strong coupling between excitons and quasibound states in the continuum in bulk transition metal dichalcogenides, *Phys. Rev. B* **107**, 045417 (2023).
- [59] *Handbook of Optical Constants of Solids*, edited by E. D. Palik (Academic Press, Cambridge, 1998), Vol. 3.
- [60] B. Li, S. Zu, Z. Zhang, L. Zheng, Q. Jiang, B. Du, Y. Luo, Y. Gong, Y. Zhang, F. Lin, B. Shen, X. Zhu, P. M. Ajayan, and Z. Fang, Large Rabi splitting obtained in Ag-WS₂ strong-coupling heterostructure with optical microcavity at room temperature, *Opto-Electron. Adv.* **2**, 190008 (2019).
- [61] V. Savinov, V. A. Fedotov, and N. I. Zheludev, Toroidal dipolar excitation and macroscopic electromagnetic properties of metamaterials, *Phys. Rev. B* **89**, 205112 (2014).
- [62] H. Li, G. Wei, H. Zhou, H. Xiao, M. Qin, S. Xia, and F. Wu, Polarization-independent near-infrared superabsorption in transition metal dichalcogenide Huygens metasurfaces by degenerate critical coupling, *Phys. Rev. B* **105**, 165305 (2022).
- [63] F. Song, B. Xiao, and J. Qin, High-*Q* multiple Fano resonances with near-unity modulation depth governed by nonradiative modes in all-dielectric terahertz metasurfaces, *Opt. Express* **31**, 4932 (2023).
- [64] L. Guo, Z. Zhang, Q. Xie, W. Li, F. Xia, M. Wang, H. Feng, C. You, and M. Yun, Toroidal dipole bound states in the continuum in all-dielectric metasurface for high-performance refractive index and temperature sensing, *Appl. Surf. Sci.* **615**, 156408 (2023).
- [65] J. A. Parker, H. Sugimoto, B. Coe, D. Eggena, M. Fujii, N. F. Scherer, S. K. Gray, and U. Manna, Excitation of nonradiating anapoles in dielectric nanospheres, *Phys. Rev. Lett.* **124**, 097402 (2020).
- [66] M. Geisler, X. Cui, J. Wang, T. Rindzevicius, L. Gammelgaard, B. S. Jessen, P. A. D. Gonçalves, F. Todisco, P. Bøggild, A. Boisen, M. Wubs, N. A. Mortensen, S. Xiao, and N. Stenger, Single-crystalline gold nanodisks on WS₂ mono- and multilayers for strong coupling at room temperature, *ACS Photon.* **6**, 994 (2019).
- [67] S. Cao, H. Dong, J. He, E. Forsberg, Y. Jin, and S. He, Normal-incidence-excited strong coupling between excitons and symmetry-protected quasi-bound states in the continuum in silicon nitride-WS₂ heterostructures at room temperature, *J. Phys. Chem. Lett.* **11**, 4631 (2020).
- [68] X. Zhang and A. L. Bradley, Polaritonic critical coupling in a hybrid quasibound states in the continuum cavity-WS₂ monolayer system, *Phys. Rev. B* **105**, 165424 (2022).
- [69] P. Törmä and W. L. Barnes, Strong coupling between surface plasmon polaritons and emitters: A review, *Rep. Prog. Phys.* **78**, 013901 (2015).
- [70] C. Tserkezis, A. I. Fernández-Domínguez, P. A. D. Gonçalves, F. Todisco, J. D. Cox, K. Busch, N. Stenger, S. I. Bozhevolnyi, N. A. Mortensen, and C. Wolf, On the applicability of quantum-optical concepts in strong-coupling nanophotonics, *Rep. Prog. Phys.* **83**, 082401 (2020).
- [71] G.-D. Liu, X. Zhai, L.-L. Wang, Q. Lin, S.-X. Xia, X. Luo, and C.-J. Zhao, A high-performance refractive index sensor based on Fano resonance in Si split-ring metasurface, *Plasmonics* **13**, 15 (2017).
- [72] T. J. Antosiewicz, S. P. Apell, and T. Shegai, Plasmon-exciton interactions in a core-shell geometry: From enhanced absorption to strong coupling, *ACS Photon.* **1**, 454 (2014).
- [73] Z. He, C. Xu, W. He, J. He, Y. Zhou, and F. Li, Principle and applications of multimode strong coupling based on surface plasmons, *Nanomaterials* **12**, 1242 (2022).
- [74] G. W. Castellanos, S. Murai, T. V. Raziman, S. Wang, M. Ramezani, A. G. Curto, and J. G. Rivas, Exciton-polaritons with magnetic and electric character in all-dielectric metasurfaces, *ACS Photon.* **7**, 1226 (2020).
- [75] F. Todisco, R. Malureanu, C. Wolff, P. A. D. Gonçalves, A. S. Roberts, N. A. Mortensen, and C. Tserkezis, Magnetic and electric Mie-exciton polaritons in silicon nanodisks, *Nanophotonics* **9**, 803 (2020).